Studying resist performance for contact holes printing using EUV interference lithography

Xiaolong Wang,* Li-Ting Tseng, Dimitrios Kazazis, Zuhal Tasdemir, Michaela Vockenhuber, Iacopo Mochi, and Yasin Ekinci
Paul Scherrer Institut, Laboratory for Micro and Nanotechnology, Villigen, Switzerland

Abstract. Extreme ultraviolet interference lithography (EUV-IL) is a relatively simple and inexpensive technique that can pattern high-resolution line/space and has been successfully used for the resist performance testing. While the aerial image in EUV-IL formed by two beams is straightforward to understand and has contrast of 1, the aerial image formed by four beams providing contact holes is rather complicated. The beam polarization and relative phases of the individual beams play a significant role in the aerial image formation in four-beam interference lithography. In particular, controlling the relative phase of the beams is very difficult to achieve due to short wavelength. To circumvent this problem, we propose an effective double exposure four-beam interference lithography method, by intentionally designing the grating with a slightly different pitch to create an optical path difference that is longer than the coherence length of the EUV light (13.5 nm). We numerically prove the effective double exposure four-beam interference is not sensitive to the phases difference and verify our analytical model by printing both positive tone chemically amplified resist and a negative tone inorganic resist. [DOI: 10.1117/1.JMM.18.1.013501]

Keywords: extreme ultraviolet; interference lithography; polarization; contact hole; chemically amplified resist.

Paper 18127 received Oct. 16, 2018; accepted for publication Dec. 14, 2018; published online Jan. 14, 2019.

1 Introduction

Contact hole (CH) patterning is an important lithography step and will be one of the key applications in extreme ultraviolet lithography. The printing of CH patterns is affected by several issues such as illumination conditions, resist, reticle, stochastics, and polarization effects.[1–4] Different methods have been used to improve the critical dimension uniformity (LCDU) of printed CHs, such as the conventional mask can be improved with phase shift mask or use the leaf hexagonal illumination technique.[2,4] Resist performance for CH patterns can be different from that of the lines/spaces and therefore needs to be addressed.

Interference lithography, exploiting the interfering interaction of coherent beams, has been developed as a cost effective and high efficient tool to fabricate periodic submicrometer structures, such as nanodots array, circular holes, chiral structures, and gratings with large scale.[5–11] Critical parameters of phase and polarization influence on the interference pattern have been addressed.[9,12–14] Although large area nanostructures could be obtained with laser interference lithography[13] and feature size down to 150 nm grating has been fabricated with UV source-based interference lithography,[7] to print higher resolution node (below 10 nm) in semiconductor industry, EUV source-based interference lithography is highly demanded for research. Synchrotron source-based EUV interference lithography has been developed and oriented to contribute to this field.[15,16]

The extreme ultraviolet interference lithography (EUV-IL) setup at the XIL-II beamline of the Swiss Light Source (SLS) has been successfully used for the resist performance testing.[16–22] It has achieved the world record line-space patterning half pitch (hp) down to 6 nm[23] in photon-based lithography. Although the aerial image for line/space patterns formed by two interfering beams is relatively simple and has 100% contrast, as it will be discussed below, the aerial image formed by four beams providing CHs is relatively complex. The image and its contrast are influenced by the phases and polarization of the interfering beams. EUV-IL is an efficient and inexpensive technique that can be used to generate CH patterns with small critical dimension (CD) and help develop new, high performance resists for future EUV nodes. It has been used to replicate hp 28 nm CHs with ZEP520A resist.[15] To leverage the full potential of this technique and to interpret the results correctly, it is important to have a thorough understanding of the aerial image formation process.

In this work, we first present the theory of aerial image formation in a four-beam interference configuration. We show that the polarization of the illumination, either transverse electric (TE) or transverse magnetic (TM), strongly influences the contrast of the aerial image, as for example in the case of two-beam interference with TE, TM, or mixed polarized beams. We then discuss the four-beam interference that is sensitive to the polarization and phase difference between the beams, which makes it extremely difficult to implement in the EUV range. To overcome this issue, we proposed an "effective double exposure four-beam" interference scheme, which is not phase sensitive as in the coherent case. We intentionally design the gratings with slightly different pitches so that the optical path difference between the two pairs of the interfering beams is longer than the coherence length of the source.[24] We call it an effective double exposure four-beam interference because the two pairs of orthogonal beams interfere independently and the intensity is summed up rather than all four beams interference each other. Also, we do only one time exposure instead of two

*Address all correspondence to Xiaolong Wang, E-mail: xiaolong.wang@psi.ch

1932-5150/2019/$25.00 © 2019 SPIE

times. This is why we call it an effective double exposure. Moreover, the four-beam mask is rotated by 45 deg ensuring that all the diffracted beams have the same mixed TE-TM polarization. Although in this case the contrast of the aerial image is lower than in the case of a double exposure (0 deg and 90 deg), the exposure is more uniform. In Sec. 3, we describe the fabrication of such four-beam masks and, in Sec. 4 we present the exposure results. We show the patterning performance of hydrogen silsesquioxane (HSQ) resist and also in a state-of-the-art chemically amplified (CAR) resist for dots and CHs patterns.

2 EUV Interference Lithography

The working principle of the EUV-IL is schematically shown in Fig. 1 for the case of two-beam interference. The transmission mask is illuminated perpendicularly with EUV light, which is plane wave and is polarized along the horizontal direction and the gratings, from the synchrotron. The light is diffracted by the two gratings and the two first-order diffracted beams interfere (with angle $\theta/2$) exactly on the surface of the photoresist-coated Si wafer. The relationship between the diffraction angle, the diffraction order, and the period of the grating is

$$\sin\theta_m = m\lambda/P, \tag{1}$$

where θ_m ($\theta/2$) is the diffraction angle, m is the diffraction order, and P is the period of the grating. Three orders (zeroth, first, and second) of diffracted beams are shown in Fig. 1(a). The zeroth-order diffracted beams do not interfere and are transmitted. The second-orders diffracted beams have a much lower diffraction efficiency and do interfere but at a smaller distance from the mask. In practice, first-order diffracted beam interference is utilized as it is easier to arrange and has relatively high diffraction efficiency.[25] The interference of the first-order diffracted beams results in a sinusoidal aerial image.

The gap between the two gratings is expressed as

$$g = \frac{d}{2\tan\theta_m}, \tag{2}$$

where g is the gap between the grating and the interference pattern (mask-wafer distance) and d is the distance between the two gratings. The aerial image formation depends on the configuration of the diffraction gratings. Line/space patterns are obtained in the two-beam interference case, while dots or CHs are obtained in the four-beam interference [Figs. 1(b) and 1(c)]. In the four-beam case, the pitch of the two pairs of gratings can be different [e.g., $p1$ and $p2$ in Fig. 1(d)]. As it will be explained later, this introduces a phase difference between the two pairs of gratings, which in turn influences the aerial image.

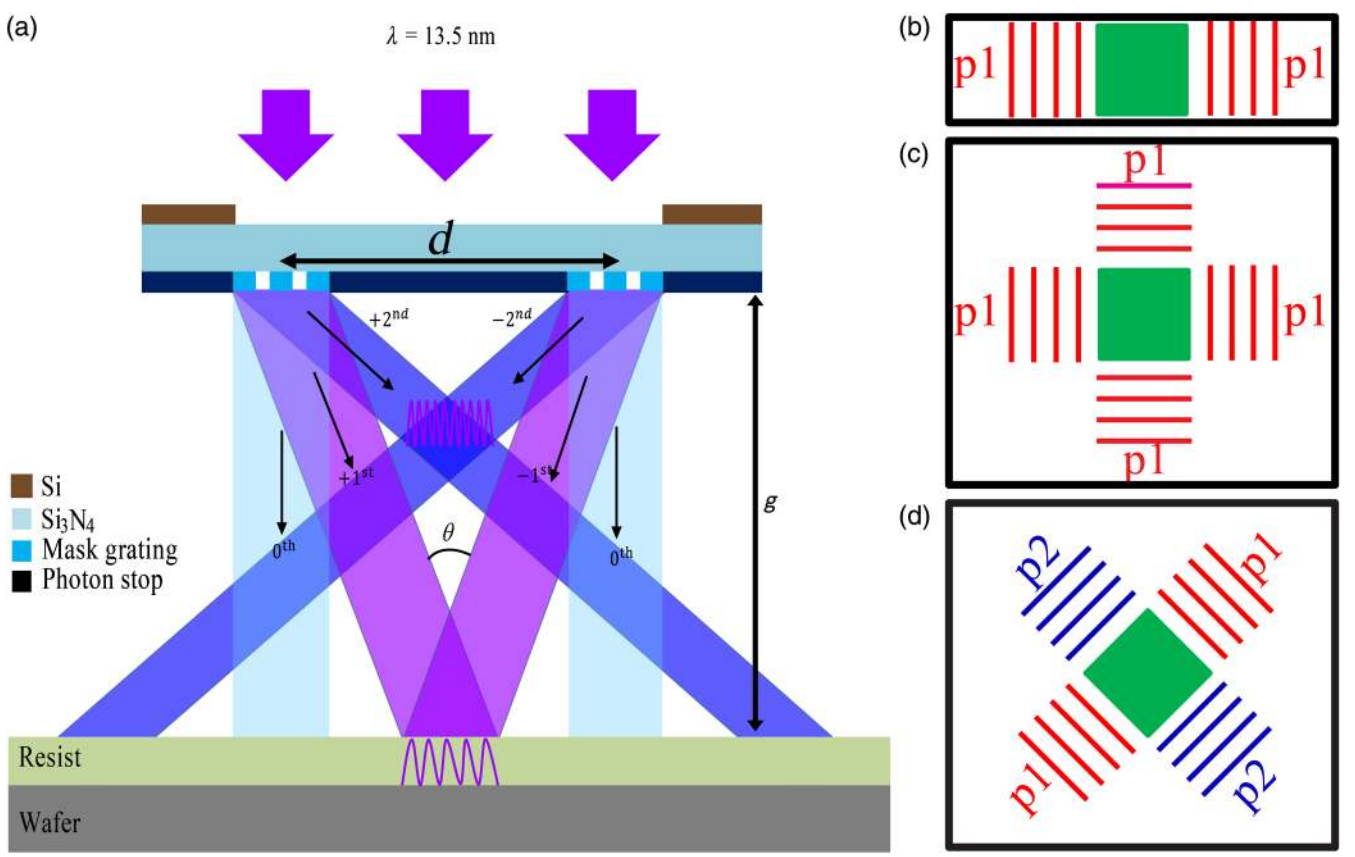

Fig. 1 (a) EUV interference lithography scheme. EUV light illuminates a transmission mask from the top. The mask consists of transmission diffraction gratings. The diffracted coherent beams form an interference pattern which is recorded in the photoresist. (b) Two-beam interference grating layout. (c) Grating arrangement for the case of coherent four-beam interference and (d) effective double exposure four-beam interference.

3 Theory of Multibeam Interference Lithography

Multibeam interference can be expressed as the supposition of the electromagnetic field vectors.[13,26,27] The electric field vector of the n'th beam is defined as

$$\vec{E}_n = A_n \vec{p}_n e^{i\vec{k}_n \bullet \vec{r}_n + \varphi_n}, \tag{3}$$

where A_n, $\vec{p}_n$, $\vec{k}_n$, $\vec{r}_n$, and φ_n are the amplitude, polarization vector, wave vector, position vector, and initial phase of the n'th beam, respectively. The polarization vector, wave vector, and position vector in Eq. (3) are expressed as

$$\begin{aligned}\vec{p}_n = &-(\cos\theta_n \cdot \cos\phi_n \cdot \cos\psi_n - \sin\theta_n \cdot \sin\psi_n)\vec{i} \\ &- (\cos\theta_n \cdot \sin\phi_n \cdot \cos\psi_n + \cos\theta_n \cdot \sin\psi_n)\vec{j} \\ &- (\sin\theta_n \cdot \cos\psi_n)\vec{k},\end{aligned} \tag{4}$$

$$\vec{k}_n = k(\sin\theta_n \cdot \cos\phi_n \cdot \vec{i} + \sin\theta_n \cdot \sin\phi_n \cdot \vec{j} - \cos\theta_n \cdot \vec{k}), \tag{5}$$

$$\vec{r}_n = x \cdot \vec{i} + y \cdot \vec{j} + z \cdot \vec{k}, \tag{6}$$

where θ_n is the incident angle, ϕ_n is the azimuthal angle, ψ_n is the polarization angle, and $k = 2\pi/\lambda$ is the wave number. The intensity of multibeam interference, the light on the photoresist which is relevant for lithography, is calculated as

$$I = \sum_{n=1}^{N} \vec{E}_n \cdot \sum_{m=1}^{N} \vec{E}_m^* = \sum_{n=1}^{N}\sum_{m=1}^{N} A_n \vec{p}_n \cdot A_m \vec{p}_m \cdot e^{[i(\vec{k}_n - \vec{k}_m)\cdot \vec{r}_n + \varphi_n - \varphi_m]}. \tag{7}$$

The polarization is critical for the two-beam interference, including two-beam with TE-TE, TM-TM, and mixed TE-TM polarization. As shown in Fig. 2(a), two TE-polarized monochromatic incident beams at angle θ interfere at the intersection. Assuming zero initial phases, equal amplitudes, and azimuthal angles $\phi_1 = 0$ deg, $\phi_2 = 180$ deg, and polarization angles are $\psi_1 = 90$ deg and $\psi_2 = 90$ deg, the electric fields are expressed as

$$\begin{aligned}E_1 &= Ae^{[i(kx\,\sin\theta - kz\,\cos\theta)]}, \\ E_2 &= Ae^{[i(-kx\,\sin\theta - kz\,\cos\theta)]}.\end{aligned} \tag{8}$$

The polarization vectors are written as

$$\vec{p}_1 = y \cdot \vec{j}, \quad \vec{p}_2 = y \cdot \vec{j}. \tag{9}$$

While the total intensity at the interference plane is

$$I = 2A^2 + 2A^2\,\cos(2kx\,\sin\theta). \tag{10}$$

An example of an aerial image of two TE-polarized beams, diffracted by two gratings 40 nm pitch, is shown as Fig. 2(g). The intensity of the white cross-section line shown in Fig. 2(g) is shown in Fig. 2(j). We note that the pitch of the aerial image is 20 nm. The conventional definition of the contrast is defined as[28]

$$V = \frac{I_{\max} - I_{\min}}{I_{\max} + I_{\min}}. \tag{11}$$

It is clear that the contrast in this case is 1.

For two TM polarized beams, the electric field is parallel to the incident plane and can be decomposed in the x and z directions regarding incident angle. In this case, assuming 0 initial phases, equal amplitudes, with the azimuthal angles $\phi_1 = 0$ deg, $\phi_2 = 180$ deg, and polarization angles $\psi_1 = 0$ deg, $\psi_2 = 0$ deg, the electric fields are

$$\begin{aligned}E_1 &= Ae^{[i(kx\,\sin\theta - kz\,\cos\theta)]}, \\ E_2 &= Ae^{[i(-kx\,\sin\theta - kz\,\cos\theta)]}.\end{aligned} \tag{12}$$

The polarization vectors are written as

$$\begin{aligned}\vec{p}_1 &= \cos\theta \cdot y \cdot \vec{i} + \sin\theta \cdot z \cdot \vec{k}, \\ \vec{p}_2 &= \cos\theta \cdot y \cdot \vec{i} - \sin\theta \cdot z \cdot \vec{k}.\end{aligned} \tag{13}$$

While obtained intensity at the interference plane is

$$I = 2A^2 + 2A^2\,\cos(2kx\,\sin\theta)\cos(2\theta). \tag{14}$$

The aerial image in this case generated with gratings pitch of 40 nm is shown in Fig. 2(h). The intensity of the white cross-section line marked in Fig. 2(h) is shown in Fig. 2(k). The contrast here is 0.77, lower than the perfect TE-polarized beams case.

The difference in contrast obtained by TE- and TM-polarized beams confirms the important role of polarization in interference. A direct control over the polarization of EUV light from a synchrotron source (SLS, Paul Scherrer Institut, Switzerland) is not as straightforward as the control of the polarization in visible light. As the polarization is determined by the transverse motion of the electrons when the electrons travel through a series undulators (magnets). The EUV light that we used in this experiment is TE polarized. We therefore indirectly change the polarization by rotating the grating by certain angle γ (e.g., 45 deg). In this case, for two-beam interference, the two diffracted beams will carry both TE and TM polarizations. The interference intensity is then calculated as

$$\begin{aligned}I = 2A^2\cos^2\gamma[2 &+ \cos(2kx\,\cos\gamma\,\sin\theta)\cos 2\theta \\ &+ 2\,\cos(2k\,\cos\gamma x\,\sin\theta)].\end{aligned} \tag{15}$$

For a grating with a pitch of 40 nm and rotated 45 deg, the intensity is plotted in Fig. 2(i). The contrast in this case, along the same line is 0.89.

It is interesting to note that the contrast in the case of the mixed TE and TM polarizations, obtained by rotating the grating to 45 deg, is actually the averaged contrast of the perfect TE- and TM-polarization cases. We calculated the contrast of the mixed TE- and TM-polarized light and compared it with perfect TE- and TM-polarized cases and the results are shown in Fig. 2(f). We also note that this mixed case is also valid for unpolarized light.

At 19-nm pitch, one can see the contrast of the TM-polarized light is zero. At 19-nm grating pitch, the diffraction angle is 45 deg, where the two incident beams have equal polarization components that are parallel and antiparallel

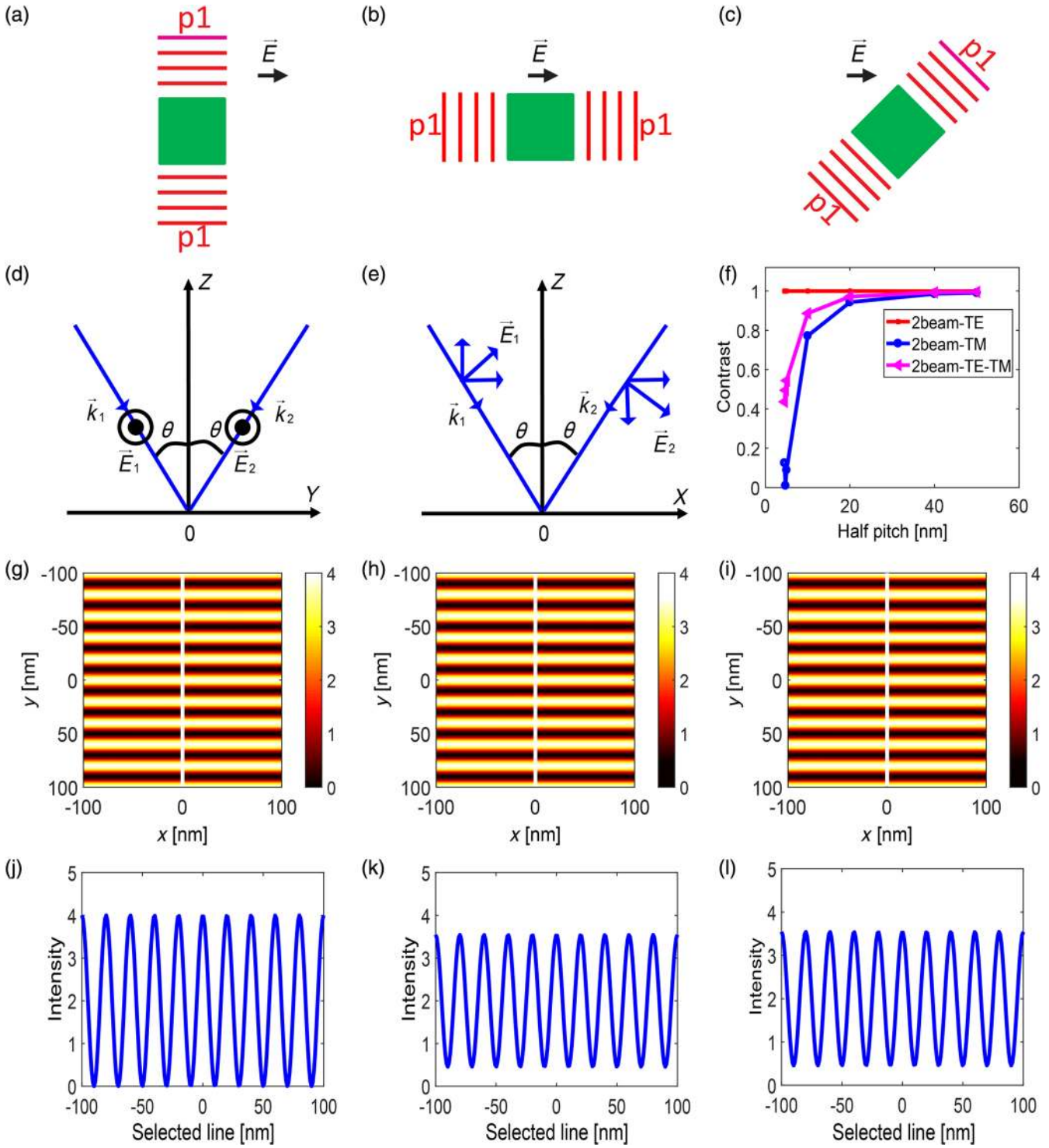

Fig. 2 Simulation of two-beam interference patterns with different polarization configurations. (a) and (b) TE polarization and TM polarization. (c) Grating rotated 45 deg with mixed TE and TM polarization. (d) and (e) Coordinate of the TE and TM polarization two-beam intersect at the center with oblique incident angle θ. (g), (h), and (i) Aerial image of lines and spaces formed with two-beam interference with TE, TM, and mixed TE and TM polarization. (j), (k), and (l) Plot of the cross section marked in (g), (h), and (i), respectively. (f) Aerial image contrast as a function of grating pitch from 20 to 200 nm with TE, TM, and mixed TE and TM polarization.

and always cancel each other. The zero-modulation at this angle is also obvious in Eq. (14).

The effect of the polarization on the contrast has been extensively discussed in the literature.[14] Here, we discuss the case for EUV and at very high-resolution patterning. As seen in Fig. 2, below a grating half-pitch of 20 nm, which corresponds to 10-nm half-pitch on wafer, the polarization effects dominate, leading to contrast loss for TM polarization and mixed polarization, i.e., unpolarized light. Such effects are valid also for conventional photolithography.

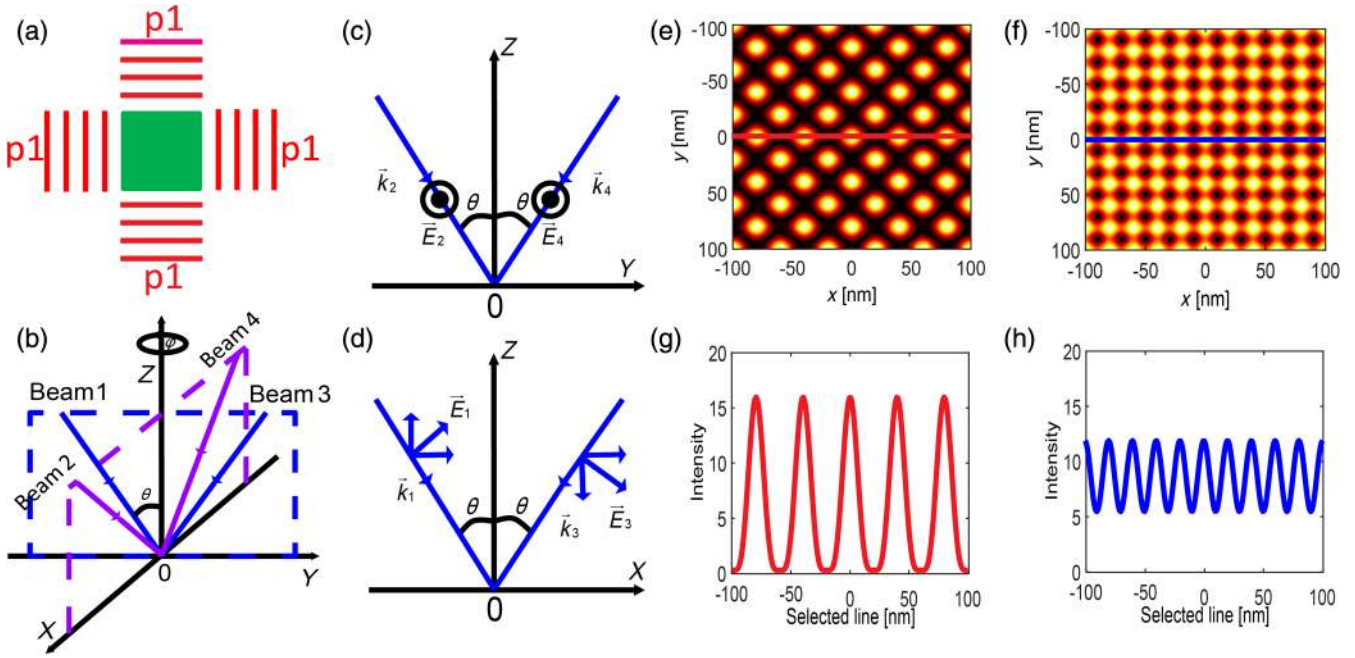

Fig. 3 Coherent four-beam interference. (a) Configuration of coherent four-beam interference with two identical grating pairs (with pitch $p1 = 40$ nm) oriented in horizontal and vertical directions. (e) Three-dimensional (3-D) Cartesian coordinate system for coherent four-beam with beam 1 and beam 3 in the *yz* plane and beam 2 and beam 4 in the *xz* plane. (b) and (f) Beam 2 and beam 4 with TE polarization while beam 1 and beam 3 have TM polarization. (c) Interference pattern with phase difference equal to $\Delta\delta = \pi$. (g) Cross-section intensity (marked red line) and the contrast in this axis is 1. (d) Interference intensity when the phase difference is $\Delta\delta = \pi/2$. (h) Intensity of the cross section marked with the blue line and the contrast is 0.33.

Whereas for two-beam interference lithography, the contrast loss can be avoided by choosing the right polarization and the relative phase difference between the interfering beams has no influence on the aerial image, in four-beam interference these factors are critical, which is the focus of this paper.

The layout of the grating-based four-beam interference lithography, which results in dots or CHs, is shown in Fig. 3(a). As shown in Fig. 3(b), beams 1 and 3 propagate in the *yz* plane and beams 2 and 4 propagate in the *xz* plane. The polarizations of the four interfering beams are shown in Figs. 3(c) and 3(d).

The electric fields for the four beams are written as following (assuming the same amplitudes for all beams, with the azimuthal angles $\phi_1 = 0$ deg, $\phi_2 = 90$ deg, $\phi_3 = 180$ deg, and $\phi_4 = 270$ deg and polarization angles are $\psi_1 = 90$ deg, $\psi_2 = 0$ deg, $\psi_3 = 90$ deg, and $\psi_4 = 0$ deg):

$$\begin{aligned} E_1 &= Ae^{[i(ky\ \sin\theta - kz\ \cos\theta)+\varphi_1]}, \\ E_2 &= Ae^{[i(kx\ \sin\theta - kz\ \cos\theta)+\varphi_2]}, \\ E_3 &= Ae^{[i(-ky\ \sin\theta - kz\ \cos\theta)+\varphi_3]}, \\ E_4 &= Ae^{[i(-kx\ \sin\theta - kz\ \cos\theta)+\varphi_4]}. \end{aligned} \tag{16}$$

The polarization vectors are written as

$$\begin{aligned} \vec{p}_1 &= \cos\theta \cdot y \cdot \vec{i} + \sin\theta \cdot z \cdot \vec{k}, \\ \vec{p}_2 &= y \cdot \vec{j}, \\ \vec{p}_3 &= \cos\theta \cdot y \cdot \vec{i} - \sin\theta \cdot z \cdot \vec{k}, \\ \vec{p}_4 &= -y \cdot \vec{j}. \end{aligned} \tag{17}$$

The intensity of the interference pattern is calculated as Eq. (18) and is shown in Fig. 3(e).

$$\begin{aligned} I = A^2\{&4 - 2\cos(2kx\ \sin\theta - 2\sigma_x) \\ &- 2(\cos 2\theta)\cos(2ky\ \sin\theta - 2\sigma_y) \\ &- \cos(\delta_x - \delta_y)4\ \cos\theta\ \cos[k\ \sin\theta(x+y) - 2\sigma_x] \\ &+ 4\ \cos\theta\ \cos[k\ \sin\theta(x+y) - 2\sigma_y]\}, \end{aligned} \tag{18}$$

where the phase related term σ_x, σ_y, δ_x, and δ_y are written as

$$\begin{aligned} \sigma_x &= \frac{(\varphi_2 + \varphi_4)}{2}, \\ \sigma_y &= \frac{(\varphi_1 + \varphi_3)}{2}, \\ \delta_x &= \frac{(\varphi_2 - \varphi_4)}{2}, \\ \delta_y &= \frac{(\varphi_1 - \varphi_3)}{2}. \end{aligned} \tag{19}$$

Particularly, two distinct interference patterns can switch from one to another when the difference satisfies

$$\Delta\delta = \delta_x - \delta_y = \begin{cases} (n + 1/2)\pi \\ n\pi \end{cases}. \tag{20}$$

From Eq. (20), one can see that the highest contrast could be obtained if the beams have zero initial phase or the phase constants that are within an even multiple of π from each other, which enable all the four beams constructively

interfere. The contrast is 1 and the aerial image pitch is $p/\sqrt{2}$ as shown in Fig. 3(e). The other case is that the relative net phase among the beams is multiple of $\pi/2$, which is similar to the effective double exposure case (shown later) as the phase sensitive term in Eq. (18) will not be existing. In this case, the resulting aerial image with pitch $p/2$ is shown in Fig. 3(f) and the contrast is significantly decreased to 0.33. One can see that the initial phase difference between two pairs of gratings significantly influences the interference pattern and its contrast as it switches from Figs. 3(e) and 3(f) when the phase change from π to $\pi/2$.

Except for these specific cases, the aerial image will not be well defined. This phase-related pattern switch shows that the coherent four-beam interference is very sensitive to the phase. One should notice it is very easy to have a $\pi/2$ phase difference in the EUV range as only a distance of half of the grating pitch (20 nm) could already provide such a phase. Even with the state-of-the-art electron beam lithography tools for research, the overlay limit is already around 10 nm. In other words, a phase difference on the order of $\pi/2$ is not very difficult to achieve and any relative alignment and placement error of the gratings will lead to an ill-defined aerial image.

Theoretically, double exposure scheme could be used to prevent loss of contrast. That would consist of using a two-grating mask and exposing twice by mounting it at 0 deg and 90 deg angles. Practically, this is time consuming and impractical due to grating misalignment caused by mounting the mask twice.

Considering all the above reasons, we adopt the method of "effective double exposure interference" where (we intentionally design the two pairs of gratings with different pitches $p1$ and $p2$ so that the optical path difference is longer than the coherence length of the EUV beam). In this case, a pair of gratings creates a two-beam interference pattern, line/spaces, whereas the other pair of gratings creates the line/spaces pattern that perpendicular to the first pair. There is no interference between the two pairs and only the intensities add up because the path difference of the beams is longer than the coherence length ($\lambda^2/\Delta\lambda$, $\lambda = 13.5$ nm, and $\Delta\lambda = 4\%$) of the EUV beam which is 337.5 nm for our tool. Even 1 nm difference between the two pitches ($p1$ and $p2$) creates 2744 nm optical path difference which is more than enough to overcome the coherent length of the beam and causes no interference.[24]

Another practical difficulty is to select the appropriate polarizations for the four-beam interference case. As shown in Fig. 2, polarization has a significant impact on the contrast, which becomes more important for the smaller pitches. In our synchrotron-based EUV-IL setup, we have a horizontal polarization and TE-polarized beam shown in Fig. 2(a) is the ideal case for two-beam interference. For four-beam interference lithography shown in Fig. 3(a), in addition to the aforementioned problem of extreme phase sensitivity, the polarization-dependent contrast leads to the anisotropic aerial image, i.e., the contrast values along the vertical and horizontal axes will be different. Moreover, diffraction efficiencies of the gratings are also different due to the polarization, which results in intensity difference between vertical and horizontal pairs of gratings and thereby leads to an anisotropic aerial image. To circumvent these problems, we rotate the gratings by 45 deg in order to have the same polarization of the light for the gratings.

The grating configuration (rotated angle $\gamma = 45$ deg) is shown in Fig. 4(a). One can imagine that the reference frame of the effective double exposure case is rotated by 45 deg with respect to the one of the coherent case. In other words, there is a rotation angle $\gamma = 45$ deg between the x axis and x' axis as shown in Figs. 4(a) and 4(f). All four beams have the same polarization (mixed TE and TM) incident light. The electric fields, polarization vectors are given as

$$\begin{aligned} E_1 &= A\cos\gamma e^{[i\cos\gamma(ky\sin\theta - kz\cos\theta)+\varphi_1]},\\ E_2 &= A\cos\gamma e^{[i\cos\gamma(kx\sin\theta - kz\cos\theta)+\varphi_2]},\\ E_3 &= A\cos\gamma e^{[i\cos\gamma(-ky\sin\theta - kz\cos\theta)+\varphi_3]},\\ E_4 &= A\cos\gamma e^{[i\cos\gamma(-kx\sin\theta - kz\cos\theta)+\varphi_4]}, \end{aligned} \tag{21}$$

$$\begin{aligned} \vec{p}_1 &= x\cdot\vec{i} + z\cdot\vec{k},\\ \vec{p}_2 &= y\cdot\vec{j} + z\cdot\vec{k},\\ \vec{p}_3 &= x\cdot\vec{i} - z\cdot\vec{k},\\ \vec{p}_4 &= y\cdot\vec{j} - z\cdot\vec{k}. \end{aligned} \tag{22}$$

For the simulations, we choose realistic pitches of $p1 = 40$ nm and $p2 = 44$ nm. The intensity of the interference pattern is calculated as Eq. (23) and shown in Fig. 4(b):

$$\begin{aligned} I = A^2\cos^2\gamma[4 &+ 2\cos(2kx\cos\gamma\sin\theta - 2\sigma_x)\cos 2\theta\\ &+ 2\cos(2k\cos\gamma y\sin\theta - 2\sigma_y)]. \end{aligned} \tag{23}$$

One can immediately notice that the effective double exposure case does not have the phase-sensitive cross-talk term as in the coherent case [see Eq. (18)]. This will give more freedom during practical implementation. The interference intensity is shown in Fig. 4(b) for the grating pitches $p1 = 40$ nm and $p2 = 44$ nm. The aerial image on the wafer level has hp 10 and 11 nm along the horizontal and vertical axes. The cross section intensity of sinusoidal plot for x axis and diagonal axis are shown in Fig. 4(e). The contrast is 0.3 and 0.85 along the x axis and the diagonal axis, which are lower than the coherent case (1 and 1). Furthermore, we can see that the minimum intensity is not zero anymore [x axis cross section intensity, blue curve in Fig. 4(e)]. There is bridging effect appearing at the transition from maximum to minimum (or from peak to valley), which means the conventional contrast definition is not able to accurately describe the transition from bright to dark of the two-dimensional (2-D) aerial image anymore. In this case, the normalized image log-slope (NILS) is a more suitable metric to describe the aerial image properties and the equation of NILS is defined as[29]

$$\mathrm{NILS} = w\frac{\mathrm{d}\ln(I)}{\mathrm{d}x}, \tag{24}$$

where w is the nominal linewidth and I is the intensity.

The NILS values [calculated with Eq. (24)] of the x axis and the diagonal axis cross section from half-pitch 10 to 50 nm are shown in Fig. 4(f).

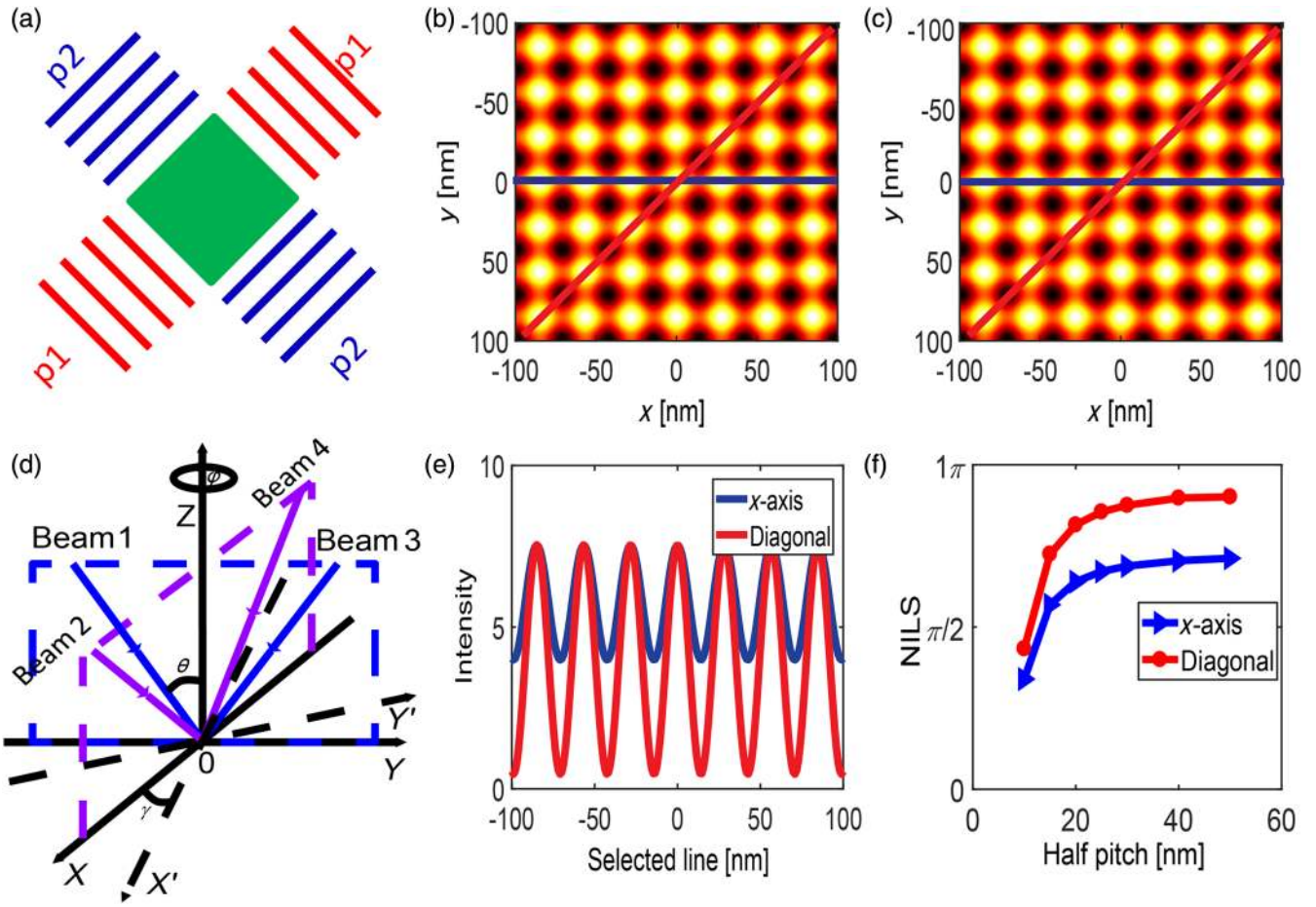

Fig. 4 Effective double exposure and grating rotated by 45 deg four-beam interference. (a) Configuration of effective double exposure four beam with two identical grating pairs (with pitch $p1 = 40$ nm and $p2 = 44$ nm) rotated by 45 deg. (d) Three-dimensional Cartesian coordinate system of effective double exposure four beams with beam 1 and beam 3 in *yz* plane and beam 2 and beam 4 in the *xz* plane. The coordinate is rotated 45 deg from the horizontal and vertical directions as in the coherent case. (b) and (e) Two-dimensional aerial image and plot of the intensity along the *x* axis and diagonal axis of the interference. (c) and (f) Two-dimensional aerial image and the NILS along the *x* axis and the diagonal axis marked by the blue and red lines for the grating half-pitch from 10 to 50 nm.

4 Fabrication of EUV-IL Masks

The grating mask fabrication process is described in detail elsewhere[16] and the process flow is shown in Fig. 5. Briefly, a 100-nm-thick silicon nitride membrane is cleaned in a short oxygen plasma (RIE 80, Oxford Instruments, United Kingdom) for 2 min at 150 W. In addition to cleaning, the oxygen plasma process also improves the adhesion of the subsequent photoresist films by spin-coating. Next, high resolution and negative tone HSQ photoresist (Fox16, Dow Corning, Midland Michigan) diluted 1:6 in methyl isobutyl ketone (MIBK) is coated by spin coating at 3000 rpm for a target thickness of ~75 nm. Using e-beam lithography (EBL) (EBPG 5000+, Vistec, Jena, Germany) 80 μm × 80 μm gratings are patterned, horizontally oriented with pitch varying from 76 to 100 nm with step of 8 nm and vertically oriented with pitch from 72 to 96 nm, with a dose of 15,000 $\mu C/cm^2$. After the exposure, the samples are developed in a NaOH developer (Microposit 351, Dow) mixed 1:3 with deionized (DI) water for 120 s, rinsed with DI water, and dried with nitrogen.

In the second step, a photon stop pattern is defined which prevents the transmission of the zeroth-order beam (see Fig. 5, step 4). For this purpose, a layer of poly methyl-methacrylate (PMMA, molecular weight 950k, Allresist GmhH, Strausberg, Germany) dissolved 4% in ethylactate (Technic France, Saint-Denis, France) was spin-coated at 2000 rpm for 45 s to target a thickness of ~400 nm. The film was baked at 175°C for 5 min on a hot plate. After alignment, all areas of the mask except the grating area were exposed at a dose of 800 $\mu C/cm^2$. The mask was then developed in a 1:1 solution of MIBK and isopropanol (IPA, Technic France) for 2 min to leave PMMA covering the grating areas on the mask. A short oxygen plasma (RIE 80, Oxford Instruments, United Kingdom) for 20 s at 40 W was used to remove the residual material on the developed patterns. The photon-stop pattern was then defined by the deposition of a Cr/Au bilayer (2 nm/20 nm) by thermal evaporation, followed by lift-off in acetone. This Cr/Au layer served as a seed layer in order to grow ~140 nm of nickel (step 6 in Fig. 5). Nickel is used because it is an excellent photon-stop material due to its high diffraction efficiency and high contrast at EUV.[30]

The completed mask was then mounted on a stainless steel mask holder using PMMA and the completed assembly installed in the XIL beamline for the interference

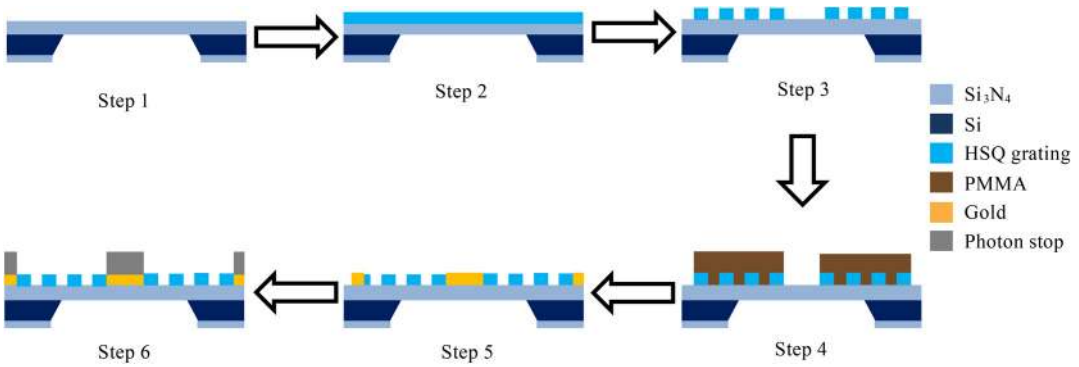

Fig. 5 Mask fabrication process flow. A Si_3N_4 membrane is spin-coated with HSQ and gratings patterned with EBL. A second e-beam overlay in PMMA followed by metal deposition, lift-off, and nickel electroplating produces the photon stop.

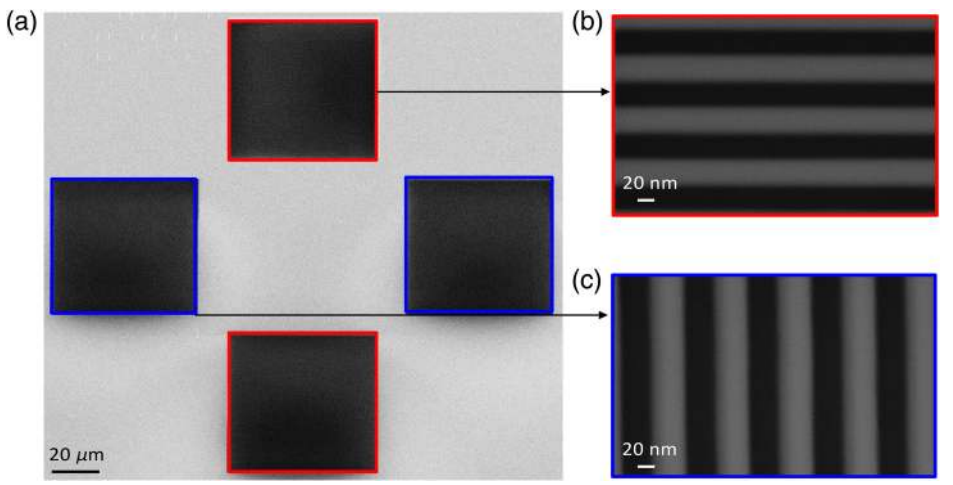

Fig. 6 SEM images of the fabricated four-beam interference grating mask. Scale bars equal 20 nm.

lithography. Figure 6 shows a scanning electron microscopy (SEM, ZEISS Supra, Jena, Germany) of the fabricated transmission diffraction gratings on silicon nitride membrane. The pair of gratings in red boxes are horizontally oriented (beam 2 and beam 4 with pitch 100 nm), while the gratings in the blue boxes are vertically oriented (beam 1 and beam 3 with pitch 96 nm).

5 EUV Exposures

The fabricated masks were tested at our EUV-IL tool. The EUV light with wavelength $\lambda = 13.5$ nm (corresponding to energy 92.0 eV) was provided by a third-generation 2.4-GeV synchrotron source (SLS, Paul Scherrer Institut, Switzerland). The beam is polarized along the horizontal direction and the gratings used for two-beam interference are aligned accordingly, providing the maximum contrast for line/space patterns. For four-beam interference, the mask is rotated to 45 deg as we shown in the theoretical part to produce an equal mix of TE and TM polarization for all the beams. The EUV-IL setup at the XIL beamline is described in detail in Ref. 16.

Two types of resists, namely, positive-tone CAR resist and negative-tone HSQ resist were tested using a four-beam interference mask. The exposure was performed on Si wafer. For the negative-tone HSQ resist XR1541 diluted 1:1 with MIBK was spin-coated at 5000 rpm to target a thickness of ~20 nm. For the positive-tone CAR resist was spin-coated at a speed 1500 rpm for 45 s to target a thickness of ~25 nm. The samples were mounted onto the motorized sample stage and the exposure was performed with photon flux 21 mW/cm^2 and doses on mask varying from 150 to 1343 mJ/cm^2 for the HSQ resist and from 10 to 90 mJ/cm^2 for the case of CAR. The HSQ resist sample was then developed in a NaOH developer (Microposit 351) mixed 1:3 with DI water for 30 s, rinsed under DI water for 60 s, and blow dried using nitrogen. The CAR sample was developed in MF26a for 30 s and DI water showered for 60 s and then dried with nitrogen. The samples were finally inspected using SEM at an acceleration voltage of 1 kV and a working distance of 3.0 mm.

The obtained patterns for HSQ (dots) and CAR (CHs) resists are shown in Figs. 7 and 8. For HSQ dots pattern, the doses were 321, 321, 342, and 342 mJ/cm^2. The printed dots for hp 24 nm down to hp 18 nm on wafer were clearly resolved at dose 38, 31.4, 34.5, and 31.4 mJ/cm^2. Although the pattern of HSQ dots is well-resolved at hp 24 nm, the HSQ dots from hp 20 nm and the CAR CHs start to show defects and nonuniformity. It can be seen that the uniformity of the patterns (both dots and CHs) decreases in higher resolution. To quantify the uniformity, we calculated

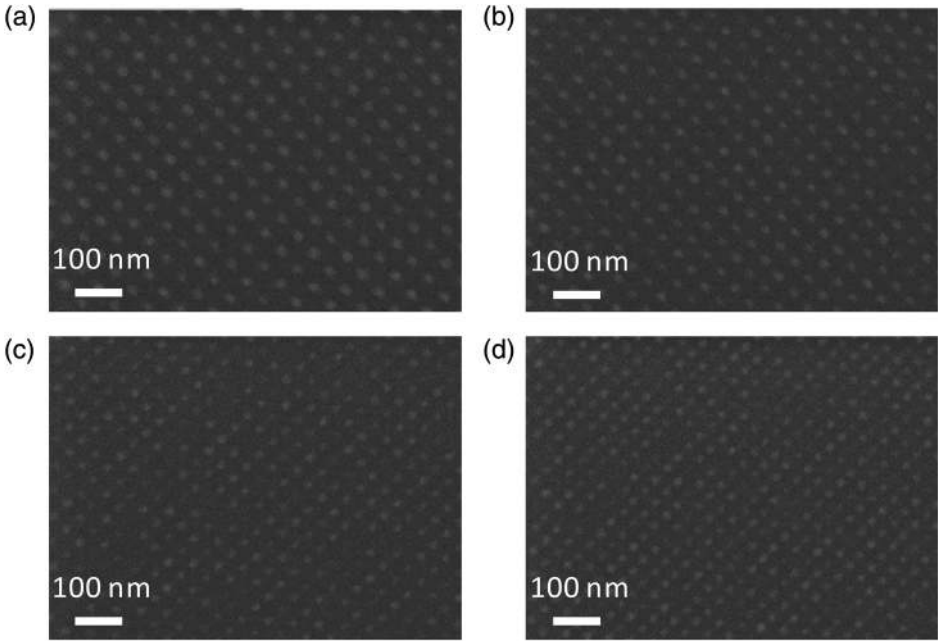

Fig. 7 Dots produced by EUV-IL onto HSQ negative tone resist on Si wafer. (a) hp 24 nm, (b) hp 22 nm, (c) hp 20 nm, and (d) hp 18 nm. (a)–(d) Scale bars: 100 nm.

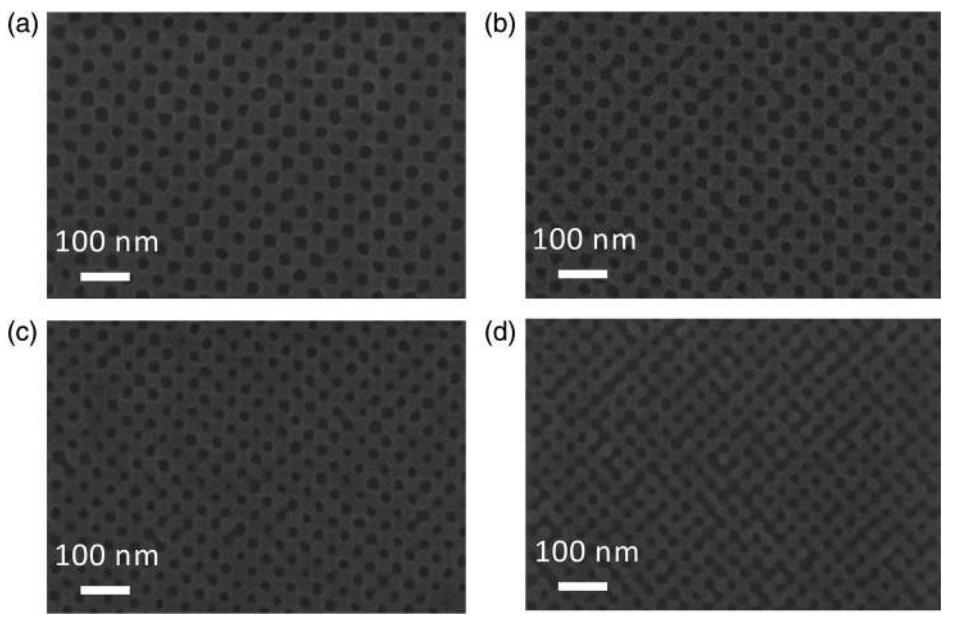

Fig. 8 CH produced by EUV-IL onto CARS positive tone resist on Si wafer. (a) hp 24 nm, (b) hp 22 nm, (c) hp 20 nm, and (d) hp 18 nm. (a)–(d) Scale bars: 100 nm.

the LCDU of CHs using a homemade software with 3 sigma standard.[31] The LCDU are 5.2, 6, 6.4, and 7.4, respectively, for hp 24 nm, hp 22 nm, hp 20 nm, and hp 18 nm, respectively.

We note that these are preliminary results and future work includes optimization of the mask fabrication process. Although we are not certain about the resolution of the CAR, HSQ shows much higher resolution than shown here. The nonuniformity of the patterns indicates that the mask fabrication was not fully successful. Further optimization of the mask making process includes improving the adhesion of HSQ resist on the membrane by promoter or prebaking of the sample. Also as four-beam interference shows higher efficiency, the resist thickness could be decreased to decrease the final aspect ratio of HSQ gratings. Pattern collapse mitigation techniques such as critical point drying can be used in order to remove the limitation of pattern collapse. As the four-beam interference is more complex than the two-beam case, any minor pattern collapse or defects in the grating would cause inhomogeneity of the printed CHs.

6 Conclusions

We discussed how the polarization of the incident light strongly influences the contrast in two-beam interference. The contrast is 1 for TE polarization and independent of the half-pitch. For TM polarization, the contrast decreases with increasing resolution which is small effect for grating pitches above and it is 0.77 for a grating pitch of 40 nm (i.e., 10 nm hp on wafer) and becomes 0 for the grating pitch 19 nm. In the case of four-beam interference lithography, the contrast loss due to the polarization effects cannot be avoided and a mixed polarization is the best option to mitigate the effects. Moreover, we demonstrated that the perfect TE-TE-TM-TM polarization four-beam interference gave the highest contrast when the phase difference between the two pairs grating is zero. However, this TE-TE-TM-TM perfectly coherent four-beam interference showed pattern switch and the contrast decreased when there was a $\pi/2$ phase difference between the two pairs of gratings. This coherent four-beam interference strongly depends on the phase difference between the two pairs of gratings. In practice, it is extremely difficult to implement in the EUV range. One reason is that the $\pi/2$ phase can easily be induced just by a half pitch of the grating (e.g., hp $= 20$ nm), which is possible even with state-of-the-art EBL tools. In addition, a small tilt of the mask or a vibration during the exposure could also easily cause a random phase difference between the two pairs of gratings. This unpredictable phase difference between the two pairs of gratings could result in ill-defined interference patterns. Therefore, we proposed an effective double exposure four-beam interference scheme with rotated gratings by 45 deg so that all the gratings have the same incident light (mixed TE-TM polarization). On one hand contrast is lost, compared to the coherent case. On the other hand, this effective double exposure four-beam interference configuration is not sensitive to the phase difference between the two pairs of gratings. In addition, single exposure is enough to print CHs with low dose as all the gratings experience the same polarization light. Finally, we fabricated our effective double exposure four-beam interference mask (HSQ grating) with EBL and tested the mask at XIL-II beamline with 13.5-nm EUV light. We printed dots pattern with negative tone HSQ resist and CHs with positive CARs resist. We observed nonuniformity of the printed patterns and assigned this to the imperfection of the mask gratings.

Acknowledgments

The authors would like to thank Markus Kropf for technical assistance. Part of the experimental work was performed at the Swiss Light Source, Paul Scherrer Institute. A version of this paper was currently under consideration for publication as an SPIE Proceedings paper.

References

1. A. A. Schafgans et al., "Performance optimization of MOPA pre-pulse LPP light source," *Proc. SPIE* **9422**, 94220B (2015).
2. P. Naulleau et al., "Ultrahigh efficiency EUV contact-hole printing with chromeless phase shift mask," *Proc. SPIE* **9984**, 99840P (2016).
3. D. Civay et al., "Deconstructing contact hole CD printing variability in EUV lithography," *Proc. SPIE* **9048**, 90483D (2014).
4. M. Lim et al., "EUV contact-hole local CD uniformity optimization for DRAM storage node application," *Proc. SPIE* **10583**, 105830X (2018).
5. X. Chen et al., "Interferometric lithography of sub-micrometer sparse hole arrays for field-emission display applications," *J. Vac. Sci. Technol. B* **14**(5), 3339–3349 (1996).
6. Y. K. Pang et al., "Chiral microstructures (spirals) fabrication by holographic lithography," *Opt. Express* **13**(19), 7615–7620 (2005).
7. G. Fuetterer et al., "Interference patterning of gratings with a period of 150 nm at a wavelength of 157 nm," *Proc. SPIE* **4691**, 1703–1713 (2002).
8. D. Xia et al., "Nanostructures and functional materials fabricated by interferometric lithography," *Adv. Mater.* **23**(2), 147–179 (2011).
9. H. Korre et al., "Development of a simple, compact, low-cost interference lithography system," *J. Vac. Sci. Technol. B* **28**(6), C6Q20–C6Q24 (2010).
10. C. Lu and R. H. Lipson, "Interference lithography: a powerful tool for fabricating periodic structures," *Laser Photonics Rev.* **4**(4), 568–580 (2010).
11. Q. Xie et al., "Fabrication of nanostructures with laser interference lithography," *J. Alloys Compd.* **449**(1), 261–264 (2008).
12. A. Fernandez and D. W. Phillion, "Effects of phase shifts on four-beam interference patterns," *Appl. Opt.* **37**(3), 473–478 (1998).
13. J. Xu et al., "Fabrication of moth-eye structures on silicon by direct six-beam laser interference lithography," *J. Appl. Phys.* **115**(20), 203101 (2014).
14. M. Totzeck et al., "How to describe polarization influence on imaging," *Proc. SPIE* **5754**, 23–37 (2004).
15. T. Urayama et al., "EUV interference lithography for 1X nm," *J. Photopolym. Sci. Technol.* **24**(2), 153–157 (2011).
16. N. Mojarad, J. Gobrecht, and Y. Ekinci, "Interference lithography at EUV and soft x-ray wavelengths: principles, methods, and applications," *Microelectron. Eng.* **143**, 55–63 (2015).
17. N. Mojarad et al., "Broadband interference lithography at extreme ultraviolet and soft x-ray wavelengths," *Opt. Lett.* **39**(8), 2286–2289 (2014).
18. Y. Ekinci et al., "Evaluation of resist performance with EUV interference lithography for sub-22-nm patterning," *Proc. SPIE* **8322**, 83220W (2012).
19. E. Buitrago et al., "SnOx high-efficiency EUV interference lithography gratings towards the ultimate resolution in photolithography," *Microelectron. Eng.* **155**, 44–49 (2016).
20. A. M. Goethals et al., "Progress in EUV resist performance," *J. Photopolym. Sci. Technol.* **19**(4), 501–506 (2006).
21. E. Buitrago et al., "Sensitivity enhancement of chemically amplified resists and performance study using extreme ultraviolet interference lithography," *J. Micro/Nanolithogr. MEMS, MOEMS* **15**(3), 033502 (2016).
22. E. Buitrago et al., "State-of-the-art EUV materials and processes for the 7 nm node and beyond," *Proc. SPIE* **10143**, 101430T (2017).
23. D. Fan and Y. Ekinci, "Photolithography reaches 6 nm half-pitch using EUV light," *Proc. SPIE* **9776**, 97761V (2016).
24. B. Terhalle et al., "Advanced holographic methods in extreme ultraviolet interference lithography," *Proc. SPIE* **8102**, 81020V (2011).
25. L. Wang et al., "Facile fabrication of high-resolution extreme ultraviolet interference lithography grating masks using footing strategy during electron beam writing," *J. Vac. Sci. Technol. B* **31**(6), 06F602 (2013).
26. M. Born and E. Wolf, *Principles of Optics: Electromagnetic Theory of Propagation, Interference and Diffraction of Light*, Pergamon Press, Oxford (1970).
27. B. E. A. Saleh and M. C. Teich, *Fundamentals of Photonics*, Wiley, Chicester (2013).
28. A. A. Michelson, *Studies in Optics*, The University of Chicago Press, Chicago (1927).
29. C. Mack, "Using the normalized image log-slope part 3," *Microlith. World* **10**, 26–27 (2001).
30. B. L. Henke, E. M. Gullikson, and J. C. Davis, "X-ray interactions: photoabsorption, scattering, transmission, and reflection at E = 50–30, 000 eV, Z = 1–92," *At. Data Nucl. Data Tables* **54**(2), 181–342 (1993).
31. A. Cohen et al., "Improving wafer level CD uniformity for logic applications utilizing mask level metrology and process," *Proc. SPIE* **8880**, 888025 (2013).

Xiaolong Wang received his PhD from EPFL, Switzerland, in 2017, working on nanophotonics. He is currently doing his postdoc at the Paul Scherrer Institute, Switzerland, since 2018. He is working on advanced lithography and nanofabrication. Also, he is working on the projects with EUV lithography industry.

Li-Ting Tseng received her PhD in 2016 from the University of New South Wales, Australia, working on diluted magnetic semiconductors. She has been working as a postdoc at the Paul Scherrer Institute, Switzerland, on advanced lithography and nanofabrication since 2017.

Dimitrios Kazazis received his PhD in 2009 from Brown University, USA, working on GeOI tunneling FETs. He did his postdoc until 2014 at CNRS-LPN near Paris, on suspended 2DEGs and quantum Hall effect metrology on graphene. He then joined the Paris Observatory developing THz detectors. Since 2016, he has been working at the

Paul Scherrer Institute, Switzerland, on advanced lithography and nanofabrication. He has taught several courses at Brown and at Paris 7 University.

Zuhal Tasdemir received her PhD in 2015 from University of Koc, Turkey, working on silicon nanowires. She has been currently doing her postdoc as Marie Curie fellow at the Paul Scherrer Institute, Switzerland, since 2017. She has been working on advanced nanofabrication for EUV resist testing and also working on silicon nanowires.

Michaela Vockenhuber has been a technician from the Laboratory for Micro- and Nanotechnology at the Paul Scherrer Institute, Switzerland, since 2009. She has been supporting all the exposures with the XIL-II lithography beamline.

Iacopo Mochi is an optical physicist. He started working on EUV mask inspection in 2008 at the Center for X-Ray Optics, where he contributed to the design and development of the SHARP microscope. Later, he joined IMEC as an R&D engineer studying SRAF solutions to mitigate EUV mask 3-D effects. In 2016, he joined the Paul Scherrer Institute where he is currently working on the development of RESCAN, an actinic pattern inspection platform.

Yasin Ekinci received his PhD from the Max Planck Institute for Dynamics and Self Organization in Göttingen, Germany, in 2003. Since 2009, he has been a senior scientist at the Paul Scherrer Institute. He is the head of the Advanced Lithography and Metrology Group at the Laboratory for Micro- and Nanotechnology. He works on EUV interference lithography and lensless imaging along with other topics in nanoscience.